Modulating CO_2 electrocatalytic conversion to organics pathway by the catalytic site dimension

Haiping Xu[ab†], Jianxin Wang[ab†], Haiying He[c*], Inhui Hwang[d], Yuzi Liu[e], Chengjun Sun[d], Haozhe Zhang[af], Tao Li[bd], John V. Muntean[a], Tao Xu[b*], Di-Jia Liu[af*]

[a]Chemical Sciences and Engineering Division, Argonne National Laboratory, Lemont, IL 60439, USA

[b]Depart-ment of Chemistry and Biochemistry, Northern Illinois University, DeKalb, IL 60115, USA

[c]Department of Physics and Astronomy, Valparaiso University, Valparaiso, IN 46383, USA

[d]X-ray Science Division, Argonne National Laboratory, Lemont, IL 60439, USA

[e]Center for Nanoscale Materials, Argonne National Laboratory, Lemont, IL 60439, USA

[f]Pritzker School of Molecular Engineering, The University of Chicago, Chicago, IL 60637, USA

[*]Email: haiying.he@valpo.edu; Email: txu@niu.edu; djliu@anl.gov

[†]H.X and J.W. contribute equally to this paper

ABSTRACT: Electrochemical reduction of carbon dioxide to organic chemicals provides a value-added route in mitigating greenhouse gas emission. We report a family of carbon-supported Sn electrocatalysts with the tin size varying from single atom, ultra-small clusters to nano-crystallite. High single-product Faradaic efficiency (*FE*) and low onset potential of CO_2 conversion to acetate (*FE* = 90 % @ -0.6 V), ethanol (*FE* = 92% @ - 0.4 V), and formate (*FE* = 91% @ -0.6 V) were achieved over the catalysts of different active site dimensions. The CO2 conversion mechanism behind these highly selective, size-modulated *p*-block element catalysts were elucidated by structural characterization and computational modeling, together with kinetic isotope effect investigation.

INTRODUCTION

Electrochemical CO2 reduction reaction (CO2RR) to form organic liquids such as ethanol, acetate, or formate offers an economic path to mitigate the greenhouse gas emission at scale when coupled with renewable but intermittent electricity generated from solar or wind. [1-14] To achieve CO2RR to various organics with high single-product selectivity at low overpotential is essential in reducing separation cost and energy consumption. However, these conversion reactions often involve escalating numbers of proton coupled electron transfers (PCET) and carbon-carbon coupling, rendering them more technically challenging compared to more robust two-electron conversion to single-carbon products such as CO [15-25]. In this study, we report the design and synthesis of a family of carbon-supported tin electrocatalysts with the metal active size systematically varying from the atomically dispersed, ultra-small

clusters to nano-crystallites. We observed nearly unit single-product selectivity of CO_2RR to acetate, ethanol, or formate at the record low overpotentials in the kinetic region modulated simply by the tin active site dimension. As an abundant *p*-block element, this study shows that tin (Sn) could serve as another low-cost alternative in the electrocatalyst materials library for CO2 conversion to multi-carbon liquid organics. Tin as a main group element augments the current transition metal-based materials with new prospect in promoting atomic orbital-molecular interaction during the catalytic reaction. Structural characterization and computational modeling revealed that carbon-carbon coupling and PCET can be modulated by the size and the electronic structures of tin, which ultimately altered the electrocatalytic CO_2RR pathways. A kinetic isotope effect (KIE) study by exchanging H2O with D2O of the electrolyte found major shift in the conversion product make-up as the function of electrochemical potentials during CO2RR.

Sn metal crystallite has been found effective in converting CO_2 to formate and CO [26-31], both are 2-electron processes without the C-C bond formation. Converting CO_2 to multi-carbon (C_{2+}) organics, however, requires significantly higher numbers of PCET (for example, 12 electrons for ethanol and 8 electrons for acetate) and C-C coupling between the reaction intermediates. In this study, we found that Sn could mechanistically achieve high *FE*s to C_2 chemicals such as acetate (*FE* = 90 % at -0.6 V), or ethanol (*FE* = 92% at - 0.4 V), in addition to formate (*FE* = 91% at -0.6 V) by simply tuning the metal site dimension through controlling the tin loading in the catalyst. All the electrochemical potentials described in this study refer to the reversible hydrogen electrode (RHE) unless otherwise indicated.

RESULTS AND DISCUSSION

We adopted our previously reported amalgamated lithium metal (ALM) synthesis method [32] and prepared a series of carbon (Vulcan XC-72) supported catalysts of different Sn dispersion and cluster size. The active center size control was achieved by applying different amounts of metallic Sn into the molten lithium (Li) during the amalgamation step (Fig. 1a, 1b, 1c). Sn was found to be uniformly dissolved and atomically dispersed at all loadings after quenching the molten lithium to solid at room temperature, determined by X-ray absorption spectroscopy (Fig. S1). After converting Li to LiOH under humidified air, the Sn/LiOH mixtures were blended with XC-72, followed by leaching away LiOH by water, transferring Sn over the carbon surface. During the transfer process, formation of additional hydroxyl and carboxyl groups occurred as the result of reactions between strong alkaline solution with carbon (Fig. S2), which helped to anchor highly dispersed Sn over carbon. All steps after quenching were performed at the ambient temperature without agglomeration. This distinctive feature is in stark contrast to

the conventional catalyst preparation method using chemical precursors followed by high temperature reduction, which often causes random metal size distribution through agglomeration.

Seven supported catalysts, Sn/C-x with nominal tin loading of x wt.% where x from 0.12 to 12, were prepared. At the lowest loading of 0.12 wt.%, Sn in Sn/C-0.12 is in a highly dispersed atomic form, as is shown by high-angle annular dark-field aberration-corrected scanning transmission electron microscopy (HAADF-STEM) (Fig. 1d). As the loading increased by ten folds to 1.2 wt.%, Sn atoms in Sn/C-1.2 start to assemble to ultrasmall clusters, while the surface of atoms remains exposed (Fig. 1e). Further increase of Sn loading by another ten folds to 12 wt.% leads to the formation of 3 to 5 nm metal crystallites in Sn/C-12, as is shown by the bright field transmission electron microscopy (TEM) [26] (Fig. 1f and Fig. S3). Powder X-ray diffraction (PXRD) detected no scattering peak from Sn related species in Sn/C-0.12 and Sn/C-1.2, consistent with the highly dispersed ultrasmall metal active sites in the absence of long-range pattern in these catalysts. In contrast, Sn metal and Sn oxides were observed in Sn/C-12, indicating the formation of large crystallites as the Sn loading increased (Fig. S4).

The coordination structures surrounding Sn in Sn/C-0.12, Sn/C-1.2 and Sn/C-12 were analyzed by the radial distribution function (RDF) extracted from the extended x-ray absorption fine structure (EXAFS) and the electronic structure of Sn in these catalysts were investigated by x-ray absorption near edge structure (XANES). The RDF of the first coordination shell of Sn in Sn/C-0.12 is predominantly Sn-O with a coordination number (CN) of 3.7 (±0.3), similar to that of Sn(II) acetylacetonate, or Sn(AcAc)2, in which tin is ligated by four oxygen (Fig. 1g, Fig. S5a, Table S1). The electronic structure of Sn in Sn/C-0.12 in XANES mimics that of Sn(AcAc)2 with tin being in +2 oxidation state (Fig. S6a). Combined coordination and electronic structures lead to a DFT simulated μ-oxo Sn-O-Sn active site which will be discussed below. As the Sn loading increased, the Sn-Sn peak appears in the RDF of Sn/C-1.2 while Sn-O peak decreased (Fig. 1h, Fig. S5b). The EXAFS analysis showed CNs of 2.1 (±0.7) for Sn-O and 2.3 (±0.4) for Sn-Sn shells (Table S1), respectively, and XANES showed a mixture of Sn(0) and Sn(II) oxidation states (Fig. S6b), suggesting the presence of ultrasmall Sn-Sn cluster (3 ~ 4 atoms) ligated by O at the exterior. Further increase of Sn loading rendered more metallic tin in the catalyst. This was reflected by the trace amount Sn-O and dominant Sn-Sn peak intensity in Sn/C-12 (Fig. 1i, Fig. S5c) with the CN of 3.2 (±1.1) for Sn-Sn (Table S1). In addition, the XANES of Sn/C-12 resembled more closely to that of Sn foil (Fig. S6c). The gradual transition from fully oxidized to nearly all reduced Sn observed by EXAFS and XANES agreed well with the HAADF-STEM results. The existence of oxygenated Sn(II) in these

catalysts is also evidenced by x-ray photoelectron spectroscopy (XPS) (Fig. S7) and Raman study (Fig. S8), respectively.

The change in Sn dispersion resulted in different active site structures which, in turn, completely altered the CO_2RR pathways. The electrocatalytic performances were evaluated by linear sweep voltammetry (LSV), cyclic voltammetry (CV) and chronoamperometry test in 0.1 M $KHCO_3$ electrolyte solution on a catalyst-coated rotating disc electrode (RDE) in a single cell and on a catalyst coated carbon paper in the cathodic chamber of a H-cell, respectively [32,33]. In comparison, RDE is more beneficial in improving mass transport and reducing unintended side reactions by uncovered carbon. LSVs over Sn/C catalysts from 0 to -1.3 V showed enhanced current densities in the CO_2 purged electrolyte over that of purged by Ar, indicating the direct CO_2RR through solvated CO_2 [34] (Fig. 2a, 2b and 2c). Similar observations were also found in the CVs between CO_2 and Ar saturated electrolytes (Fig. S9). As a baseline comparison, the electrode containing XC-72 treated by the same ALM process except without adding Sn yielded much lower current density with H_2 being the dominant product. No C_2 compounds was observed (Fig. S10 and Fig. S11). Fig. 2d showed the *FE*s of the direct CO_2RR product distributions and total current densities at applied potentials from -0.4 V to -1.2 V over Sn/C-0.12. The NMR identified acetate as the predominant chemical in the electrolyte (Fig. S12a) with its *FE* reaching 90.0% at a low potential of -0.6 V, representing a record of direct electrocatalytic conversion of CO_2-to-acetate. The partial current density for acetate formation at -0.6 V is listed in Table S2. The catalyst maintained stable current at different cell potentials from -0.3 to -1.2 V (Fig. S13a) during the chronoamperometric measurements and the *FE* for acetate was found nearly constant over an extended period of 26 hours (Fig. S13d).

As Sn loading in the catalyst increased to 1.2 %, the makeup of the CO_2 conversion products altered significantly. Fig. 2e shows the *FE*s for CO_2RR product distributions as the function of cell potentials from -0.3 V to -1.2 V over Sn/C-1.2 and ethanol was found to be the major product detected by NMR (Fig. S12b). The onset potential for ethanol formation as low as -0.3 V was observed with a decent *FE* of ~ 32%. The *FE* for ethanol reached 92% at -0.4 V, representing the highest value for direct CO_2-to-ethanol conversion at the lowest overpotential reported by the literature. Very good catalyst stability measured at different current densities was also demonstrated at various potentials from -0.3 to -1.2 V (Fig. S13b) and *FE* of conversion to ethanol was found nearly constant over an extended period of 26 hours (Fig. S13e). To validate the long-term catalyst stability at high potential therefore high current density, we also measured the CO_2RR on Sn/C-1.2 at -1.0 V for 20 hours. The result still shows the stable *FE*s although the dominant product was formate at this potential (Fig. S14).

Further increase of Sn loading by another factor of

10 pivots CO_2RR catalysis yet to another path. Fig. 2f shows the *FE*s and product distributions at the applied potentials from -0.3 V to -1.2 V over Sn/C-12. Formate now represents the main product from the NMR analysis (Fig. S12c). The onset potential for formate formation as low as -0.3 V was detected with a *FE* of ~ 26%, and the *FE* increased to 91% at -0.6 V. Chronoamperometry study found the excellent catalyst stability at various potentials from -0.3 to -1.2 V (Fig. S13c) and *FE* maintained nearly constant over a 22-hour span at -0.6 V (Fig. S13f). Our observation of the effective conversion of CO_2 over large crystallite Sn is consistent with previous studies. [26,29]

We should point out an important observation that, under more negative cell potential, formate becomes the dominate product during CO_2RR over all these catalysts. As we will discuss below, this could be attributed to the impact of conversion path under higher reaction rate.

ALM synthesis offered a versatile control and continuous tunability of the metal dispersion in the catalyst. To understand the transition between different CO_2RR mechanisms as the metal dispersion changes, the catalysts with nominal Sn loadings of 0.54 wt.% (Sn/C-0.54), 0.71 wt.% (Sn/C-0.71), 2.6 wt.% (Sn/C-2.6) and 4.3 wt.% (Sn/C-4.3) were also studied (Supporting Materials and Methods). For each catalyst, LSVs and CVs in CO_2 and Ar purged electrolyte (Fig. S15), *FE*s, electrochemical surface area (ECSA, Table S3) and the product distribution, as well as chronoamperometry at different electrode potentials were measured (Figs. S16, S17, S18, S19). LSVs over these catalysts showed the rise of CO_2RR current density with the incremental increase of the Sn loading, as one would have expected. The *FE*s and CO_2RR product distribution at different potentials, however, revealed changing trends as the Sn loading thereby the metal dispersion varied. To this end, we produced three 3-dimensional contour plots between *FE*, cell potential and the Sn loading for CO_2RR to acetate, ethanol and formate, respectively (Fig. 3a, 3b, 3c).

The *FE* for acetate formation shows a sharp, "spire-shaped" peak at ca. 90% with a narrow potential window centered at -0.6 V at the lowest Sn loading (0.12 wt.%). The *FE* response for the conversion to ethanol becomes broader with a "hill-shaped" contour. While the highest *FE* of 92% already occurs at the onset potential of -0.4 V and declines relatively slowly with the decrease of the cell voltage, the Sn loading centers at 1.2 wt.% with broader width compared to that in acetate. Finally, the FE response to the formate formation has a "slope-shaped" contour of a broad cell voltage window. The preferred Sn loading is at the high end of 12 wt.%, opposite to that of acetate and ethanol formations. Note that this size-modulated conversion selectivity in Sn-based catalysts is very different from that observed for Cu-based catalysts. High CO2RR to ethanol was achieved under low Cu loading with atomically dispersion. However, the increase of the Cu active site dimension at higher metal loading caused the formation of a mixture

of multiple compounds without a dominant single product *FE*.[32]

We also drew the Tafel plots for the formation of acetate, ethanol and formate over the catalysts with different Sn loadings (Fig. 3d, 3e, 3f) and obtained the reaction rates from the Tafel slopes through linear extrapolation over the "kinetic region" (Table S4 and Table S5). For CO_2RR to acetate, the Tafel plot of Sn/C-0.12 separates from the others. It shows the lowest Tafel slope (168 mV/dec), therefore the highest kinetic rate at lower overpotential (η) compared to others. For CO_2RR to ethanol, the Tafel plot of Sn/C-1.2 has the lowest slope (175 mV/dec) and it groups closely with those of Sn/C-2.6 and Sn/C-4.3. For CO_2RR to formate, Sn/C-12 shows the lowest overpotential and the highest current density despite that the Tafel slope is similar to others. The increase of overpotential is seen as the loading of Sn decreases in the catalyst. The Tafel plot study suggests that kinetics of CO_2RR to all three organics is also sensitive to Sn size. Among these Tafel plots, Sn/C-0.12 that has the highest *FE* for CO_2-to-acetate conversion, exhibits the lowest slope thus fastest rate (Fig.3d), while Sn/C-1.2 that has the highest *FE* for CO_2-to-ethnaol conversion, shows the lowest slope thus the fastest rate (Fig. 3e).

The electrocatalyst activities measured by RDE for various catalysts were also repeated in the H-cell study. Since the anodic and cathodic chambers are separated by an anionic exchange membrane (Selemion AMV), H-cell measurement excludes the concern that the organics produced at the working electrode may undergo a secondary oxidation at the counter electrode, as that could possibly occur in RDE. In our experiment, one side of the carbon paper was coated by CO_2RR catalyst whereas the other side was sealed by watertight epoxy to minimize the hydrogen formation over the uncovered portion of the paper at high-reductive potential. We repeated the measurements of the conversion product distributions and *FE*s and found them in general agreement with the RDE results except at high-negative potentials (Fig. S20). We attribute this difference to two possible causes: one is from limited CO_2 concentration in the electrolyte therefore insufficient mass transfer to catalyst layer at higher overall reaction rates; the other one is from the residual gas production promoted by carbon alone at the edge of the carbon paper that cannot be fully sealed by the epoxy.

To decipher the nature of the active sites, *in situ* X-ray absorption spectroscopy (XAS) (EXAFS and XANES) at Sn K-edge were carried out to probe the electronic and coordination structures of the Sn catalyst under CO_2RR potentials in an *operando* electrochemical cell containing 0.1 M $KHCO_3$ solution purged by flowing CO_2 [32]. Data for Sn/C-1.2 and Sn/C-12 were acquired and analyzed whereas Sn/C-0.12 was not due to its metal loading too low to generate suitable data quality. XANES and EXAFS analyses of Sn/C-1.2 under the open circuit voltage (OCV) in the presence of CO2 purging indicates that Sn is in +2 oxidation

state coordinated by 3.3 (±0.3) oxygen. (Fig. S21a and b, Table S6), which is higher than 2.1 in the "as-synthesized" catalyst (Table S1). We ascribe this to the additional oxidation and water ligation during the ink preparation by ultrasonication at ambience, which insert O into Sn-Sn bond, leading to increased Sn-O coordination. Upon initiating CO_2RR to ethanol at -0.4 V and to further lowering the potential to -0.9 V, Sn(II) gradually reduces to Sn(0) reflected by decreasing "white-line" intensity and formation of Sn-Sn shell with CN to 2.4 (Table. S7), almost restored to 2.3 in the "as synthesized" catalyst (Table S1). Similar effect was also found on Sn/C-12 sample after ink processing, which led to the oxidation at the Sn metal cluster surface. XANES and EXAFS show that a significant fraction of Sn was already in the metallic form at OCV (Fig. S21c, Fig. S21d). By applying cell potential to -0.6 V and subsequently to -1.0 V, more Sn(II) are reduced to Sn(0) and CN of Sn-Sn increased to 4.8, indicating that metallic Sn as the active center for the conversion to formate (Table. S7). Structural characterizations of XAS of the electrocatalysts through 20-hour CO2RR were also evaluated after the samples were taken out of the H-cell (Fig.S22). As an example, we also conducted a post-mortem HAADF STEM study on Sn/C-1.2 (Figure S23) and found a similar morphology to that of "as synthesized" catalyst shown in Fig. 1e.

To understand the electrocatalytic mechanism behind the size modulated CO_2RR selectivity, we studied the catalytic pathways over the corresponding active sites of these three representative catalysts using density function theory (DFT). Representative Sn structural models (Fig. S24) were built on hydroxylated graphene surface based on the XAS studies. Under the ultralow loading (Sn/C-0.12), only Sn-O but no Sn-Sn bond was applied to construct a Sn_2O_2 cluster model with a μ-oxo Sn-O-Sn structure, based on the ex-situ XAS study (Fig. 1g, Fig. S6a, Table S1). The calculated equilibrium distance between two Sn atoms is this μ-oxo complex is 3.29 Å with tin being in +2 oxidation state. Higher CN observed for Sn-O shell than that described by the model in the "as synthesized" Sn/C-0.12 can be ascribed to adsorption by H_2O to the unsaturated Sn in the complex. These H_2O could be replaced by the adsorbate species during CO_2 reduction (See Fig. S25), and vice versa, therefore were not included in the model.

For Sn/C-1.2 of higher metal loading, a model consisting of triatomic Sn cluster bonded by two O from the hydroxylated graphene, Sn_3O_2, was proposed. The active site contains both metallic Sn(0) and oxidized Sn (II) with highly under-coordinated Sn-Sn bonds, consistent with both EXAFS and XANES analyses (Fig. 1h and Fig. S6). These modelled structures are fully relaxed and found to be stable energetically, in comparison with other structural variations (Fig. S26, Table S8).

Under very high tin loading (Sn/C-12), Sn takes the form of metallic nanoparticles with size ranging from 3 ~ 5 nm. We expect it behaves similarly to Sn metal, where

we choose Sn (001) surface to simulate its catalytic activity. Since CO_2RR to formate over metallic Sn has been well studied [32], our calculation has focused on conversion mechanism for C-C coupling over the ultralow and medium Sn loading catalysts.

Gibbs free energies for the most thermodynamically favorable reaction pathways of forming acetate and ethanol under different cell potentials were calculated for Sn/C-0.12 and Sn/C-1.2, respectively (Fig. 4). Competitive pathways together with all the corresponding structures of intermediate states are also presented (Fig. S27, Fig. S28, Fig. S29, Fig. S30, Fig. S31 and Table S9). For Sn/C-0.12, the limiting potential UL of forming CH_3COOH over Sn2O2@G is calculated to be -0.82 V (Fig. 4a), which is by far more favored than the formation of CH_3CH_2OH over Sn2O2@G (UL = -1.61 V, Fig. S32, Fig. S33). The formation of these C2 products is featured by sequential reduction of two CO2. The first CO2 is reduced as HCOO* forming a bidentate binding configuration with the two Sn atoms (Fig. 4d) in the Sn_2O_2 cluster, whose energy is significantly lower than that of COOH* (Fig. 4c). After three more ($H^+ + e^-$) pair transfer, HCOO* is reduced to H_2CO* with only one oxygen binding to one Sn atom (Step 5). This computation-postulated intermediate is experimentally validated by using H_2CO as the feeding reactant in electrocatalytic reduction reaction (see Supporting Materials and Methods, and Fig. S34). The second CO_2 is now reduced and adsorbed as COOH* with its C atom binding to an O atom bridging the two Sn atoms in the cluster. The C-C coupling occurs as $H2CO^* + COOH^* \rightarrow OCH_2COOH^*$ (Step 6), leading to the formation of CH_3COOH with an activation barrier Ea of 0.54 eV (between Step 6 and 7). The intermediate, COOH*, is critical for acetate formation. Note that the second CO_2 cannot bind in a stable HCOO* form.

To form CH_3CH_2OH, COOH* needs to be further reduced. The elementary step $COOH^* + H^+ + e^- \rightarrow CO^* + H_2O$ turns out to be the rate limiting step with an endothermic free energy change of 1.61 eV (Fig. S32, Fig. S33. Fig. S27 shows the comparison of the HCOO* and COOH* pathways for Sn_2O_2@G catalyzed CO2 reduction, indicating HCOO* is the slightly more favorable based on thermodynamics. In contrast, the supported Sn_3O_2 cluster does not show any feasible pathway to CH3COOH. Despite that the free energy of the adsorbate HCOO* is much lower than that of COOH* (Fig. 4c), the overall rate limiting potential favors the COOH* pathway (Fig. S29 and Fig. S30) of the sequential reduction of two CO_2 (Fig. 4b). The rate limiting step is the removal of the OH* group: $OH^* + H^+ + e^- \rightarrow H_2O$ with UL = -0.73 V, which is more favorable than that of the HCOO* pathway (UL = -0.95 V for the step $H_3CO^* + HCOO^* + H^+ + e^- \rightarrow H_3CO^* + HCOOH^*$). The C-C coupling occurs as $HCO^* + CO^* \rightarrow HCOCO^*$ with an activation barrier Ea of 0.35 eV (from Step 6 to 7). Although the rate limiting (maximum energy uptake) steps are identified to be later steps on the reaction pathways presented in Fig. 4, i.e. step 7→8 (0.82 eV) for the reactions on

Sn_2O_2@G and step 14→15 (0.73 eV) on Sn_3O_2@G. There are energy demanding steps equally important occur at much earlier steps, step 4→5 (0.77 eV, $H_2COOH^* \rightarrow H_2CO^*$) for the reactions on Sn_2O_2@G and step 5→6 (0.72 eV, $HCO^* + COOH^* + H^+ + e^- \rightarrow HCO^* + CO^* + H_2O$) for the reactions on Sn_3O_2@G. For high loading such as Sn/C-12, formate is the primary product as demonstrated by our Sn (001) surface model (Fig. S35), as previously reported for Sn metals [32]. The free energy change of forming bidentate HCOO* on Sn (001) is relatively low (-0.21 eV, Fig. 4c), which leads to a low limiting potential of -0.51 V to form $HCOO^-$ (aq). On the other hand, the weak binding also inhibits the formation of multi-carbon products, because strong binding between the unsaturated metal sites and reaction intermediate at proximity is essential to complete multiple ($H^+ + e^-$) transfers and C-C coupling [35,36]. Under the low Sn loadings (modelled by Sn_2O_2@G and Sn_3O_2@G), our study identified that the strong binding through unsaturated Sn and/or O centers leads to the energetically more favorable reduction beyond HCOOH under relatively low potentials (0.7~0.8 V), and the competing among C-C coupling and surface HCOOH desorption may dictate the selectivity towards C_2 products (Figs. S36, S37). These calculated mechanisms agree well with our experimental observation on the general trend in product selectivity.

The DFT calculation also provides an important insight on our experimental discovery. In analyzing acetate versus ethanol formation, the model shows a strong dependence of the catalytic pathway on the size of Sn active site. In CO_2RR to acetate, the active site is two bidentate Sn atoms ligated by one bridging O and one anchoring O. Such unique site can only form at very low Sn concentration and will transform quickly to Sn cluster as the loading increases, therefore should have a narrow range of catalytic selectivity and sharp *FE* response profile as the function of the catalyst loading, as is seen by the "spire-shaped" peak in Fig. 3a. In CO_2RR to ethanol, a triatomic Sn cluster model was proposed in our simulation. In fact, a similar result may also likely be obtained when the cluster is replaced by a tetratomic Sn moiety (the calculation not shown) etc., when the cluster contains highly exposed Sn atom with unsaturated ligation site. The concentration of Sn in the catalyst therefore could have slightly broader range, as is reflected by the "hill-shaped" contour in Fig. 3b. As Sn loading grows higher, the ratio of uncoordinated edge atoms over those at the crystallite surface decreases rapidly and becomes insignificant as the metal loading further increases. The catalytic activity will be dominated by the atoms on the lattice surface at a wide range of Sn concentration at higher loading, shown by the "slope" in Fig. 3c.

Another important insight derived from the DFT calculation is the product distribution at high-negative potentials. A rapid increase of the formate formation after potential lowered to -0.8 V and beyond was found over both

Sn/C-0.12 (Fig. 2d) and Sn/C-1.2 (Fig. 2e) catalysts, respectively. This observation is in fact consistent with our DFT calculations, which shows the formate formation is competing with both acetate and ethanol (Table S10) and the branching reaction to formic acid occurs at step 4 along the reaction coordinate (Fig. S36 and Fig. S37).

Although the formate formation is less energetically preferred compared to forward reactions to form acetate or ethanol, it does have nearly zero energy barrier and can complete the catalytic process after the desorption of formic acid. At low-negative potential, the conversion number at each active site per unit time, or turnover frequency (TOF), is low, and the catalysis can follow more energetically preferred paths along the reaction coordinate to complete C-C coupling and acetate or ethanol formation. At high negative potential, however, TOF accelerates, and the resident time required for the multiple PCET steps needed for C_2 chemical formation becomes too long compared to the more robust two proton/electron path for the formic acid formation, which can also terminate the reaction by desorption to the end-product. Although the partial current densities for both acetate and ethanol formation continuously increase as the cell potential becomes more negative (Fig. 2d and 2e), the branching reaction to formic acid accelerates even faster, which releases the reaction intermediate bottleneck by shortchanging to a two-electron process and subsequently alters to the overall conversion product mix. The more negative the potential is, the faster TOF is, and the more branching to formate occurs. To quantify the branching rate, or reaction path for that matter, requires more detailed kinetic study, which is beyond the scope of this work.

As an initial experiment to probe the PCET in CO_2RR kinetics, we conducted a kinetic isotope effect (KIE) study by replacing H_2O with D_2O in the electrolyte and re-measured *FE*s over Sn/C-0.12 and Sn/C-1.2 around the voltages for optimal acetate and ethanol formations. Interestingly, we found that, by simply switching from H_2O to D_2O while keeping other experimental conditions unchanged, led to complete alterations of the CO_2RR product makeups. In the case of Sn/C-0.12, the dominant conversion product gradually shifted from acetate (8 H^+/e^- pair transfer) to formate (2 D^+/e^- pair transfer) as potential became more negative (Fig. S38a), whereas for Sn/C-1.2, the main product switched from ethanol (12 H^+/e^- pair transfer) to acetate (8 D^+/e^- pair transfer) (Fig. S38b), respectively. In both cases, conversions to the products using less protons and electrons take over, signifying a major influence on the PCET electrocatalytic trajectory.

This observation shed a very interesting light behind the CO_2RR kinetics. Although in-depth theoretical and experimental interrogations are beyond the scope of the current work, we postulated a simple kinetic argument based on the recent development in PCET transition state theory. [38,39] KIE originates from the difference between proton and deuteron in tunneling probabilities due to the

overlap of reactant and product proton/deuteron wavefunctions. Deuterium bond in the transition state complex (D-Complex) has a reduced mass nearly twice as large of that of hydrogen bond (H-Complex), leading to narrow quantum level spacing and higher population of excited vibrational states. The vibrational frequency of H-Complex ($\nu_{H\text{-}C}$) should be ~ $2^{1/2}$ faster than that in D-Complex ($\nu_{D\text{-}C}$). In a classical sense, this could be interpreted that the forward reaction of capturing another proton-electron pair at the transition state is faster in H_2O compared to D_2O electrolyte, when other chemical environments remain the same. Such a rate difference should occur at every PCET step along the reaction coordinate, leading to the preferential formation of molecule requiring higher number of H^+/e^- pair transfers (ethanol) in H2O compared to that of requiring lower number (acetate) in D2O when the difference in kinetic barriers between the competing paths are low. A table of KIEs for the formation of ethanol, acetate and formate as the function of cell potential over Sn/C-1.2 is provided (Table S11)

These observations on altering CO_2RR pathways by slightly changing cell potential or by using deuterated water are highly intriguing. They suggest the existence of multifaceted reaction trajectories at energy levels very close to each other, as are shown by the examples of our DFT calculations (Fig. S36 and S37). Such observations are very new, only found in the CO_2 electrocatalytic conversion with multiple PCETs. We anticipate this study will trigger more follow-up theoretical and experimental studies in understanding the complexity of the CO_2RR reaction pathways.

CONCLUSIONS

We demonstrated in this study that the paths of the electrochemical conversion of CO_2 to organics, including C_2 chemicals such as acetate and ethanol, can be modulated by the dimension of Sn active sites with very high selectivity (*FE* > 90%) and low onset potentials. The new ALM synthesis offered a unique low temperature method of preparing the Sn catalysts with continually tunable active center size, leading to multiple 3-D response contours between *FE*, catalyst loading and operating potential; and their transitions from one to another. Advanced structural characterization, combined with computational modeling, revealed the nature of the catalyst site, reaction intermediates and energetics as the catalytic mechanism. Furthermore, the free energy diagram, conversion pathways under different cell potentials, as well as KIE suggest that they could impact the electrocatalysis trajectory in the complicated reaction networks during CO_2RR toward C_2 chemicals. Direct conversion to C_{2+} organics with high *FE* and low overpotential represents an important direction of integrating CO_2 as the future feedstock in the chemical production while reducing its environmental impact to the global climate change. Our study provided several insights on the catalytic mechanism which could stimulate future

exploration on new CO_2RR catalyst design and synthesis,

as well as the conditions for kinetics enhancement.

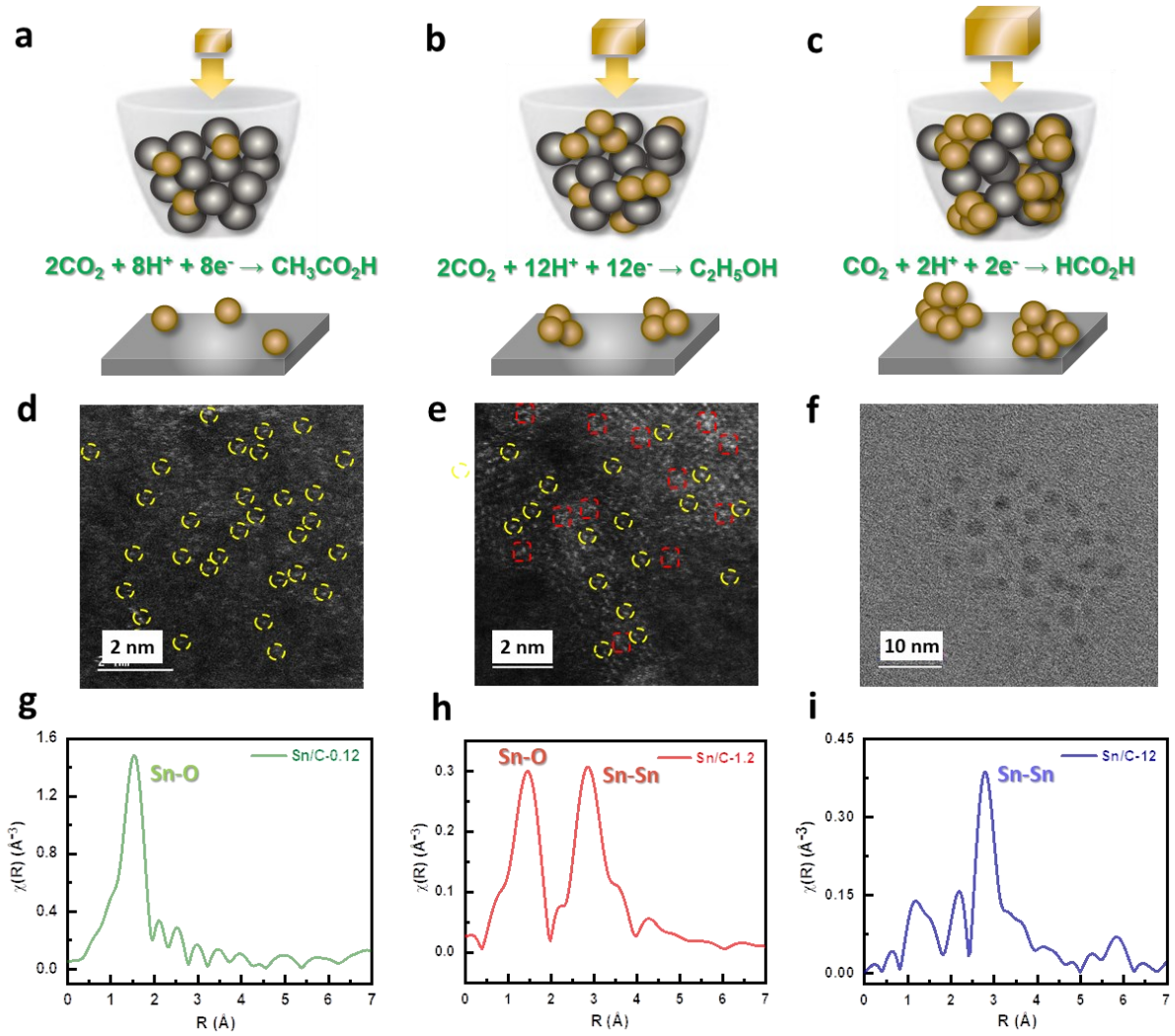

Figure 1. Syntheses of Sn/C catalyst with different metal dispersion using ALM method leading to the catalysts with high selectivity of CO_2 conversion to (a) acetate, (b) ethanol and (c) formate: HAADF-STEM images (d) Sn/C-0.12, (e) Sn/C-1.2 and bright field TEM image of (f) Sn/C-12, showing the migration from the isolated Sn atoms (in yellow circles) to the ultrasmall Sn clusters (in red circles), and to Sn nano-crystallites; Radial distribution functions from EXAFS analysis of Sn/C-0.12 (g), Sn/C-1.2 (h) and Sn/C-12 (i).

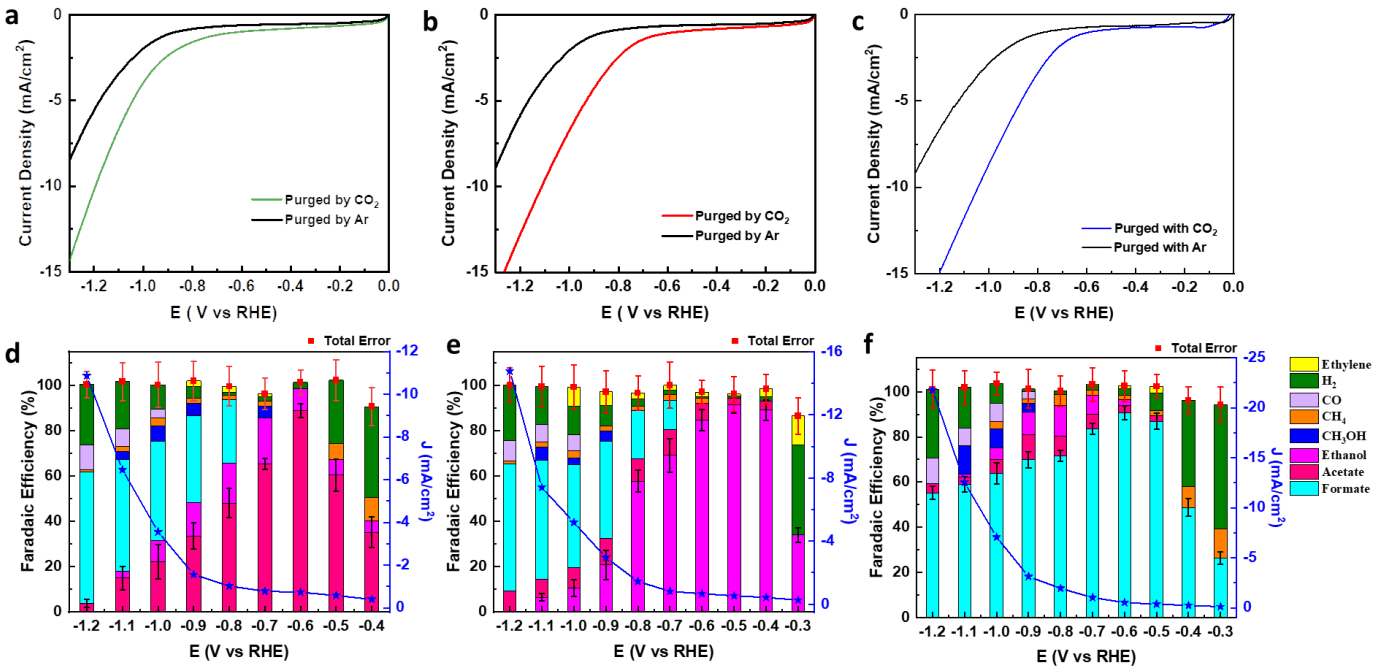

Figure 2. Electrocatalytic CO2RR measurement. LSVs of (a) Sn/C-0.12, (b) Sn/C-1.2, and (c) Sn/C-12 in Ar and CO_2 saturated 0.1 M $KHCO_3$ from 0 to -1.3 V (scan rate: 2 mV/s); *FE*s and the product distributions under different polarization potentials over (d) Sn/C-0.12, (e) Sn/C-1.2, and (f) Sn/C-12 (stacked bar chart) and the geometric partial current densities, J, toward (d) acetate, (e) ethanol, and (f) formate formation (blue line-stars). Red bars represent the combined standard errors from all the product measurements while the black bars indicate the standard errors for acetate, ethanol and formate measurements, respectively. All *FE*s are calculated from chronoamperometry measurements.

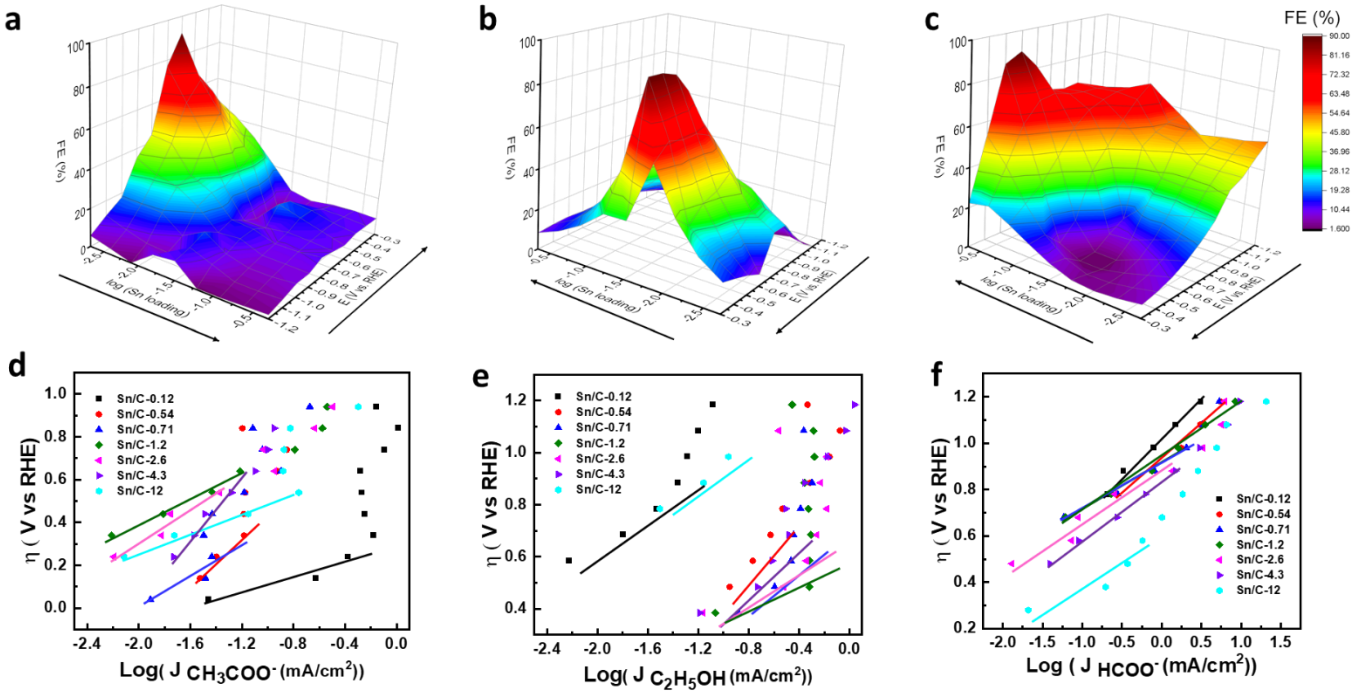

Figure 3. Dependence of CO_2RR selectivity and kinetics on the operating potential and Sn loading. 3-dimensional plots of *FE* as the functions of Sn loading and operating potential for the formation of (a) acetate over Sn/C-0.12, (b) ethanol over Sn/C-1.2 and (c) formate over Sn/C-12. Tafel plots of the formation of (d) acetate, (e) ethanol and (f) formate over the catalysts of different Sn loadings.

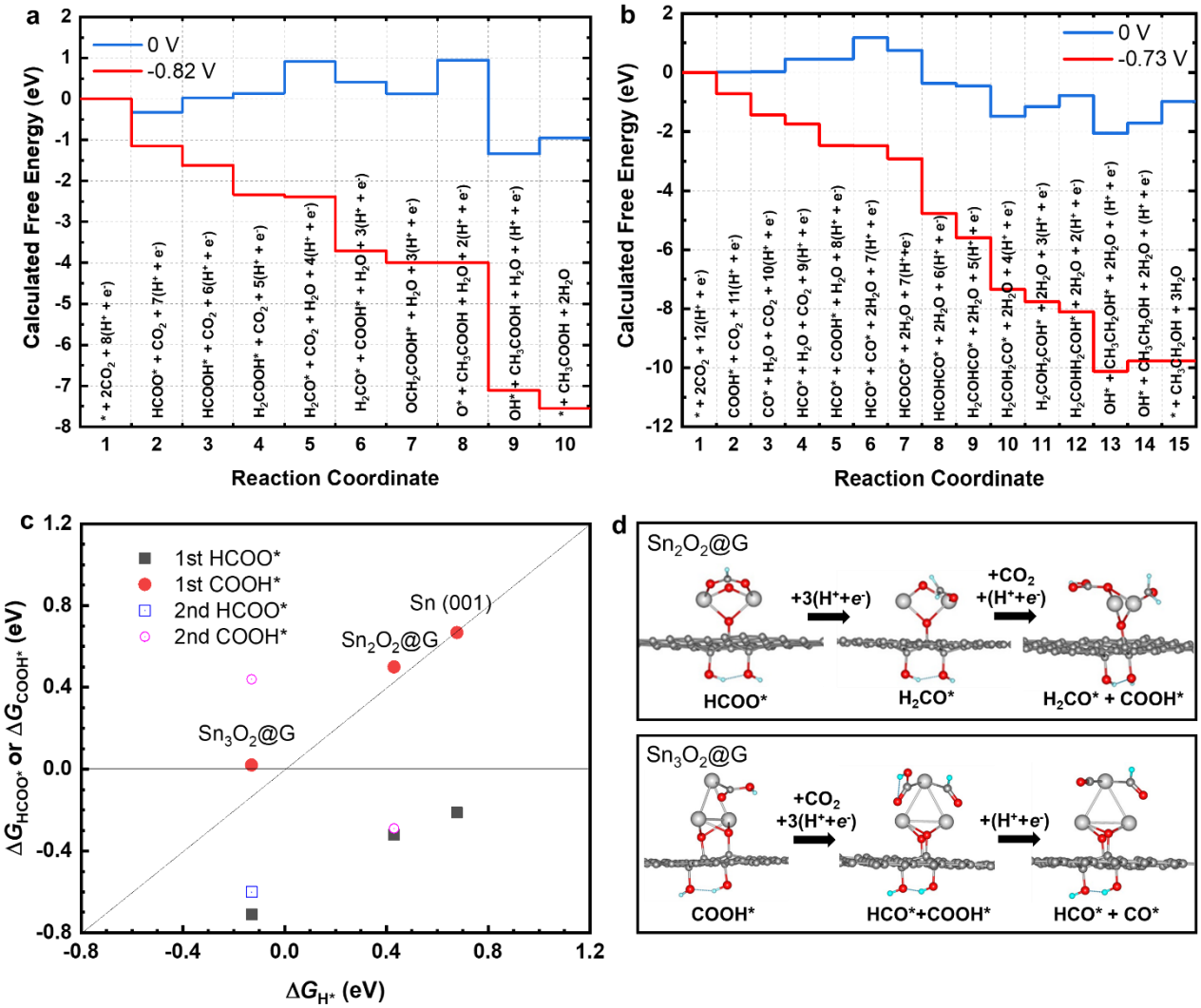

Figure 4. DFT calculations. (a) Calculated reaction pathway of electrochemical reduction of CO2 to acetic acid on Sn_2O_2@G at 0 V and -0.82 V applied voltage. (b) Calculated reaction pathway of electrochemical reduction of CO2 to ethanol on Sn_3O_2@G at 0 V and -0.73 V applied voltage. "*" denotes the catalytic site. All the electrochemical reaction steps involve transfer of a ($H^+ + e^-$) pair to the reaction site. (c) Calculated free energies of first hydrogenation of CO_2 to form HCOO* (ΔGHCOO*) or COOH* (ΔGCOOH*) vs. ΔGH*. Results are presented for both the first and the second CO_2 molecule. (d) Calculated structures of important intermediates for forming acetic acid on Sn_2O_2@G and ethanol on Sn_3O_2@G. Symbols: C in gray (small), Sn in gray (large), O in red, H in blue.

ASSOCIATED CONTENT

Supporting Information. Materials and Methods, Supporting Figures S1 to S37, Supporting Tables S1 to S10. This material is available free of charge via the Internet at http://pubs.acs.org.

Notes

The authors declare no competing interests.

ACKNOWLEDGMENT

This material is based on work supported by the U.S. Department of Energy's Office of Energy Efficiency and Renewable Energy (EERE) under the Advanced Manufacturing Office (AMO) Award Number DE-EE0009418 and Laboratory Directed Research and Development funding from Argonne National Laboratory, provided by the Director, Office of Science, of the US Department of Energy (DOE) under contract no. DE-AC02-06CH11357. The works performed at Argonne National Laboratory's Center for Nanoscale Materials and Advanced Photon Source, US DOE Office of Science User Facilities, were supported by the U.S. DOE, Office of Basic Energy Sciences, under Contract No. DE-AC02-06CH11357. The views expressed herein do not necessarily represent the views of the U.S. Department of Energy or the United States Government. Purchase of the NMR spectrometer used to obtain partial results included in this publication was supported by the National Science Foundation under the MRI award CHE-2117776.

REFERENCES

1. Hepburn, C., Alden, E., Beddington, J., Carter, E. A., Fuss, S., Dowell, N. M., Minx, J. C., Smith, P., Williams, C. K. The technological and economic prospects for CO2 utilization and removal, Nature 2019, 575, 87-97.

2. Badiani, V. M., Casadevall, C., Miller, M., Cobb, S. J., Manuel, R. R., Pereira, Ines A. C., Reisner, E. Engineering Electro- and Photocatalytic Carbon Materials for CO2 Reduction by Formate Dehydrogenase, J. Am. Chem. Soc. 2022, 144, 14207–14216.

3. Trickett, C. A., Helal, Aasif., Al-Maythalony, B. A., Yamani, Z. H., Cordova, K. E., Yaghi, O. M. The chemistry of metal–organic frameworks for CO2 capture, regeneration and conversion. Nat. Rev. Mater. 2017, 2, 17045–17060.

4. Wang, X., Wang, Z. Y., García de Arquer, F. P., Dinh, C.-T., Ozden, A., Li, Y. C., Nam, D. H., Li, J., Liu, Y. S., Wicks, J., Chen, Z. T., Chi, M. F., Chen, B., Wang, Y., Tam, J., Howe, J. Y., Proppe, A., Todorović, P., Li, F. W., Zhuang, T. T., Gabardo, C. M., Kirmani, A. R., McCallum, C., Hung, S. F., Lum, Y. W., Luo, M. C., Min, Y. M., Xu, A., O'Brien, C. P., Stephen, B., Sun, B., Ip, A. H., Richter, L. J., Kelley, S. O., Sinton D., Sargent, E. H. Efficient electrically powered CO2-to-ethanol via suppression of deoxygenation, Nat. Energy 2020, 5, 478-486.

5. Tollefson, J. Sucking carbon dioxide from air is cheaper than scientists thought, Nature 2018, 558, 173.

6. Nielsen, D. U., Hu, X. M., Daasbjerg, K., Skrydstrup, T. Chemically and electrochemically catalyzed conversion of CO2 to CO with follow-up utilization to value-added chemicals. Nat. Catal. 2018, 1, 244–254.

7. Nitopi, S., Bertheussen, E., Scott, S. B., Liu, X., Engstfeld, A. K., Horch, S., Seger, B., Stephens, I. E. L., Chan, K., Hahn, C., Nørskov, J. K., Jaramillo, T. F., Chorkendorff, I. Progress and Perspectives of Electrochemical CO2 Reduction on Copper in Aqueous Electrolyte, Chemical Reviews 2019, 119, 7610-7672.

8. Bondue, C. J., Graf, M., Goyal, A., Koper, M. T. M. Suppression of Hydrogen Evolution in Acidic Electrolytes by Electrochemical CO2 Reduction, J. Am. Chem. Soc. 2021, 143, 279–285.

9. Gao, D. F., Aran-ais, R. M., Jeon, H. S., Cuenya, B. R. Rational catalyst and electrolyte design for CO2 electroreduction towards multicarbon products, Nat. Catal. 2019, 2, 198-210.

10. Huang, J. E., Li, F. W., Rasouli, A. S., Garcia de Arquer, F. P., Liu, S. J., Zhang, S. Z., Luo, M. C., Wang, X., Lum, Y. W., Xu, Y., Bertens, K., Miao, R. K., Dinh, C. T., Sinton, D., Sargent, E. H. CO2 electrolysis to multicarbon products in strong acid, Science 2021, 372, 1074-1078.

11. Chen, X. Y., Chen, J. F., Alghorailbi, N. M., Henckel, D. A., Zhang, R. X., Nwabara, U. O., Madsen, K. E., Kenis, P. J. A., Zimmerman, S. C., Gewirth, A. A. Electrochemical CO2-to-ethylene conversion on polyamine-incorporated Cu electrodes, Nature Catal. 2021, 4, 20-27.

12. Li, Y. F., Kim, D., Louisia, S., Xie, C. L., Kong, Q., Yu, S. M., Lin, T., Aloni, S., Fakra, S. C., Yang, P. D. Electrochemically scrambled nanocrystals are catalytically active for CO2-to-multicarbons, Proc. Natl. Acad. Sci. U.S.A., 2020, 117, 9194–9201.

13. Ma, W. C., Xie, S. J., Liu, T. T., Fan, Q. Y., Ye, J. Y., Sun, F. F., Jiang, Z., Zhang, Q. H., Cheng, J., Wang, Y. Electrocatalytic reduction of CO2 to ethylene and ethanol through hydrogen-assisted C–C coupling over fluorine-modified copper, Nature Catal. 2020, 3, 478–487.

14. Hu, X. M., Daasbjerg, K. Molecular catalyst converts carbon dioxide to methanol, Nature 2019, 575, 598-599.

15. Guo, W. W., Tan, X. X., Bi, J. H., Xu, L., Yang, D. X., Chen, C. J., Zhu, Q. G., Ma, J., Tayal, A., Ma, J. Y., Huang, Y. Y., Sun, X. F., Liu, S. J., Han, B. X. Atomic Indium Catalysts for Switching CO2 Electroreduction Products from Formate to CO, J. Am. Chem. Soc. 2021, 143, 18, 6877–6885.

16. Xia, C., Zhu, P., Jiang, Q., Pan, Y., Liang, W. T., Stavitsk, E., Alshareef. H. N., Wang, H. T. Continuous production of pure liquid fuel solutions via electrocatalytic CO2 reduction using solid-electrolyte devices, Nat. Energy 2019, 4, 776-785.

17. Ren, S. X., Joulie, D., Salvatore, D., Torbensen, K., Wang, M., Robert, M., Berlinguette, C. P. Molecular electrocatalysts can mediate fast, selective CO2 reduction in a flow cell, Science 2019, 365, 367-369.

18. Gu, J., Hsu, C. S., Bai, L. C., Chen, H. M., Hu, X. L. Atomically dispersed Fe3+ sites catalyze efficient CO2 electroreduction to CO, Science 2019, 364, 1091–1094.

19. Fan, L., Xia, C., Yang, F. Q., Wang, J., Wang, H. T., Lu, Y. Y. Strategies in catalysts and electrolyzer design for electrochemical CO2 reduction toward C2+ products, Science adv. 2020, 6 (8), 3111.

20. Li, F. W., Thevenon, A., Rosas-Hernandez, A., Wang, Z. Y., Li, Y. L., Gabardo, C. M., Ozden, A., Dinh, C. T., Li, J., Wang, Y. H., Edwards, J. P., Xu, Y., MaCallum, C., Tao, L. Z., Liang, Z. Q., Luo, M. C., Wang, X., Li, H. H., Obrien, C. P., Tan, C. S., Nam, D. H., Quintero-Bermudez, R., Zhuang, T. T., Li, Y. G. C., Han, Z. J., David Britt, R., Sinton, D., Agapie, T., Peters, J. C., Sargent, E. H., Molecular tuning of CO2-to-ethylene conversion, Nature 2020, 577, 509-514.

21. Wu, Y. S., Jian, Z., Lu, X., Liang, Y. Y., Wang, H. L. Domino electroreduction of CO2 to methanol on a molecular catalyst, Nature 2019, 575, 639-642.

22. Masel, R. I., Liu, Z. C., Yang, H. Z., Kaczur, J. J., Carrillo, D., Ren, S. X., Salvatore, D., Berlinguette, C. P. An industrial perspective on catalysts for low-temperature CO_2 electrolysis, Nature Nanotechnology 2021, 16, 118–128.

23. Solla-Gullon, J., Merino-Garcia, I., Albo, J., Leguey, V., Irabien, A. Cu oxide/ZnO-based surfaces for a selective ethylene production from gas-phase CO_2 electroconversion, J. CO_2 Util. 2019, 31, 135-142.

24. Merino-Garcia, I., Albo, J., Irabien, A. Tailoring gas-phase CO_2 electroreduction selectivity to hydrocarbons at Cu nanoparticles, Nanotechnology 2017, 29, 014001.

25. Roh, I., Yu, S., Lin, C. K., Louisia, S., Cestellos-Blanco, S., Yang, P. D., Photoelectrochemical CO_2 Reduction toward Multicarbon Products with Silicon Nanowire Photocathodes Interfaced with Copper Nanoparticles, J. Am. Chem. Soc. 2022, 144, 18, 8002–8006.

26. Li, L., Ozden, A., Guo, S. Y., Garcıa de Arquer, F. P., Wang, C. H., Zhang, M. Z., Zhang, J., Jiang, H. Y., Wang, W., Dong, H., Sinton, D., Sargent, E. H., Zhong, M. Stable, active CO_2 reduction to formate via redox-modulated stabilization of active sites, Nature Commun. 2021, 12, 5233.

27. Zhao, Y., Liang, J. J., Wang, C. Y., Ma, J. M., Wallace, G. G. Tunable and efficient tin modified nitrogen-doped carbon nanofibers for electrochemical reduction of aqueous carbon dioxide, Adv. Energy Mater. 2018, 8, 1702524.

28. Li, Q., Fu, J. J., Zhu, W. L., Chen, Z. Z., Shen, B., Wu, L. H., Xi, Z., Wang, T. Y., Lu, G., Zhu, J. J., Sun, S. H. Tuning Sn-Catalysis for electrochemical reduction of CO_2 to CO via the core/shell Cu/SnO_2 structure, J. Am. Chem. Soc. 2017, 139, 12, 4290–4293.

29. Yang, Z. N., Oropeza, F. E., Zhang, K. H. P-block metals-based (Sn, In, Bi, Pb) electrocatalysts for selective reduction of CO_2 to formate, APL Materials 2020, 8, 060901.

30. Guo, J. Y., Zhang, W. L., Zhang, L. H., Chen, D. T., Zhan, J. Y., Wang, X. L., Shiju, N. R., Yuet, F. S. Control over Electrochemical CO_2 Reduction Selectivity by Coordination Engineering of Tin Single-Atom Catalysts, Adv. Sci. 2021, 8, 2102884.

31. Wang, J. G., Ning, S. L., Luo, M., Xiang, D., Chen, W., Kang, X. W., Jiang, Z., Chen, S. W. In-Sn alloy core-shell nanoparticles: In-doped SnOx shell enables high stability and activity towards selective formate production from electrochemical reduction of CO_2, Applied Catalysis B: Environmental 2021, 288, 119979.

32. Xu, H. P., Rebollar, D., He, H. Y., Chong, L., Liu, Y. Z., Liu, C., Sun, C. J., Li, T., Muntean, J. V., Winans, R. E., Liu, D. J., Xu, T. Highly selective electrocatalytic CO_2 reduction to ethanol by metallic clusters dynamically formed from atomically dispersed copper, Nat Energy 2020, 5, 623–632.

33. Zheng, T. T., Jiang, K., Ta, N., Hu, Y. F., Zeng, J., Liu, J. Y., Wang, H. T. Large-Scale and Highly Selective CO_2 Electrocatalytic Reduction on Nickel Single-Atom Catalyst, Joule 2019, 3, 265–278.

34. Feaster, J. T., Shi, C., Cave, E. R., Hatsukade, T., Abram, D. N., Kuhl, K. P., Hahn, C., Nørskov, J. K., Jaramillo, T. F. Understanding selectivity for the electrochemical reduction of carbon dioxide to formic acid and carbon monoxide on metal electrodes, ACS Catal. 2017, 7, 4822-4827.

35. Mariano, R. G., Mckelvey, K., White, H. S., Kanan, M. W. Selective increase in CO_2 electroreduction activity at grain-boundary surface terminations, Science 2017, 358, 1187-1192.

36. Liu, X. Y., Schlexer, P., Xiao, J. P., Wang, L., Sandberg, R. B., Tang, M., Brown, K. S., Peng, H. J., Ringe, S., Hahn, C., Jaramillo, T. F., Nørskov, J. K., Chan, K. pH effects on the electrochemical reduction of CO(2) towards C2 products on stepped copper, Nat. Commun. 2019, 10, 32.

37. Montoya, J. H., Tsai, C., Vojvodic, A., Nørskov, J. K. The Challenge of Electrochemical Ammonia Synthesis: A New perspective on the role of nitrogen scaling relations, Chemsuschem. 2015, 8, 2180-2186.

38. Tyburski, R., Liu, T. F., Glover, S., Hammarström, L. Proton-Coupled Electron Transfer Guidelines, Fair and Square, J. Am. Chem. Soc. 2021, 143, 2, 560–576.

39. Weinberg, D. R., Gagliardi, C. J., Hull, J. F., Murphy, C. F., Kent, C. A., Westlake, B. C., Paul, A., Ess, D. H., McCafferty, D. G., Meyer, T. J. Proton-coupled electron transfer, Chem. Rev. 2012, 112, 7, 4016–4093.

SYNOPSIS TOC